The Astrophysical Journal, 995:202 (10pp), 2025 December 20 https://doi.org/10.3847/1538-4357/ae1ca6

Unveiling the Nature of Superorbital Modulation of SMC X-1 Using NinjaSat

Chin-Ping Hu[1], Naoyuki Ota[2,3], Takuya Takahashi[2,3], Tomoshi Takeda[4], Teruaki Enoto[5,6], Toru Tamagawa[7,3,2], Biswajit Paul[8], Sota Watanabe[2,3], Wataru Iwakiri[9], Tatehiro Mihara[7], Amira Aoyama[2,7], Satoko Iwata[2,3], Kaede Yamasaki[2,3], Takayuki Kita[9], Soma Tsuchiya[2], and Mayu Ichibakase[10]
(NinjaSat collaboration)
[1] Department of Physics, National Changhua University of Education (NCUE), Changhua 50007, Taiwan; cphu0821@gm.ncue.edu.tw
[2] Department of Physics, Tokyo University of Science, 1-3 Kagurazaka, Shinjuku, Tokyo 162-8601, Japan
[3] RIKEN Nishina Center, 2-1 Hirosawa, Wako, Saitama 351-0198, Japan
[4] Graduate School of Advanced Science and Engineering, Hiroshima University, 1-3-1 Kagamiyama, Higashi-Hiroshima, Hiroshima 739-8526, Japan
[5] Department of Physics, Kyoto University, Kitashirakawa Oiwake, Sakyo, Kyoto 606-8502, Japan
[6] RIKEN Center for Advanced Photonics (RAP), 2-1 Hirosawa, Wako, Saitama 351-0198, Japan
[7] RIKEN Pioneering Research Institute (PRI), 2-1 Hirosawa, Wako, Saitama 351-0198, Japan
[8] Raman Research Institute, Astronomy and Astrophysics, C.V. Raman Avenue, Bangalore 560080, Karnataka, India
[9] International Center for Hadron Astrophysics, Chiba University, 1-33 Yayoi, Inage, Chiba 263-8522, Japan
[10] Department of Physics, Rikkyo University, 3-34-1 Nishi Ikebukuro, Toshima-ku, Tokyo 171-8501, Japan
Received 2025 September 1; revised 2025 October 29; accepted 2025 November 4; published 2025 December 17

Abstract

We report a long-term, high-cadence timing and spectral observation of the X-ray pulsar SMC X-1 using NinjaSat—a 6U CubeSat in low-Earth orbit—covering nearly a full superorbital cycle. SMC X-1 is a high-mass X-ray binary exhibiting a 0.7 s X-ray pulsar and a nonstationary superorbital modulation with periods ranging from approximately 40 to 65 days. Its peak luminosity of 1.3×10^{39} erg s^{-1} makes it a local analog of ultraluminous X-ray pulsars powered by supercritical accretion. We find that the spinup rate during the high state remains consistent with the long-term average, with no significant correlation between the spinup rate and flux. This result indicates that the modulation is primarily geometric rather than accretion-driven. The hardness ratio and spectral shape are stable throughout the entire superorbital cycle, supporting obscuration by optically thick material or energy-independent scattering. In addition, the 2–20 keV pulse profile varies with superorbital phase, which may be explained either by a variable covering fraction, due to geometric obscuration, or by free precession of the neutron star. This represents the first complete measurement of the spinup rate and spectral evolution across a single superorbital cycle in SMC X-1, highlighting the scientific capability of CubeSat-based observatories.

Unified Astronomy Thesaurus concepts: High energy astrophysics (739); Compact objects (288); Neutron stars (1108); High mass x-ray binary stars (733)

1. Introduction

SMC X-1 is an accreting X-ray pulsar in a high-mass X-ray binary system with a Roche-lobe-filling supergiant companion star (A. P. Reynolds et al. 1993; A. van der Meer et al. 2007). The pulsar has a spin period of approximately 0.7 s (frequency $\nu = 1.4$ Hz) and a variable spinup rate of around 2.5×10^{-11} Hz s^{-1} (R. Lucke et al. 1976; S. Ínam et al. 2010; C.-P. Hu et al. 2019). SMC X-1 is an eclipsing binary with an orbital period of 3.89 days, which is decreasing over time at a rate of $\dot{P}_{\rm orb} \approx 3.8 \times 10^{-8}$ (P. Wojdowski et al. 1998; M. Falanga et al. 2015; C.-P. Hu et al. 2019). This source also displays quasi-periodic superorbital modulation in the X-ray band, with the modulation period varying between roughly 40 and 65 days (e.g., D. E. Gruber & R. E. Rothschild 1984; W. I. Clarkson et al. 2003b). Notably, "excursion" events, during which the superorbital modulation period evolves to approximately 40 days for 1 to 2 yr, have been observed at least four times (W. I. Clarkson et al. 2003b; S. Trowbridge et al. 2007; C.-P. Hu et al. 2011, 2019, 2023; K. C. Dage et al. 2019).

It has long been suggested that the superorbital modulation of SMC X-1, similar to a couple of X-ray binaries like Her X-1 and LMC X-4 (see, e.g., W. I. Clarkson et al. 2003a; P. Charles et al. 2008), is caused by the obscuring of the central compact object by the radiation-driven warped or tilted accretion disk (J. E. Pringle 1996; G. I. Ogilvie & G. Dubus 2001). As long as the accretion disk undergoes precession, its warped regions can periodically obscure the line of sight to the neutron star (NS), with the modulation period corresponding to the precession period of the disk. Differences in the pulse profile shapes and changes in the relative phases between soft X-rays (below 2 keV) and hard X-rays (above 2 keV) support the presence of a warped inner-disk structure in SMC X-1 (J. Neilsen et al. 2004; R. C. Hickox & S. D. Vrtilek 2005; M. C. Brumback et al. 2020, 2023). Possible spectral hardening during superorbital transition phases has also been observed, which may be explained by increased absorption near the warped regions of the disk (S. Trowbridge et al. 2007; C.-P. Hu et al. 2011, 2019). Recent spectral analysis with NICER reveals a high partial covering fraction, further supporting the scenario in which superorbital modulation arises from substantial obscuration (R. Karam et al. 2025).

In addition, the high luminosity of SMC X-1, approximately 5×10^{38}–1.3×10^{39} erg s^{-1}, makes it a valuable local analog of extragalactic ultraluminous X-ray (ULX) pulsars (P. Pradhan et al. 2020). Several ULX pulsars—including M82 X-2 (A. K. H. Kong et al. 2016; M. Brightman et al. 2019), NGC 5907 ULX-1 (D. J. Walton et al. 2016; F. Fürst et al. 2023), and M51 ULX-7 (G. Vasilopoulos et al. 2020)—also exhibit superorbital modulations similar to those observed in

SMC X-1. However, in ULX pulsars, these modulations are often attributed to the variations in the mass accretion rate. In the most extreme case, ULX pulsars may enter the so-called "propeller" regime during their superorbital low states, where accretion is inhibited by a centrifugal barrier (A. F. Illarionov & R. A. Sunyaev 1975). If this occurs, the steady accretion torque on the NS would cease, leading to a significantly reduced spinup rate or even a considerable spindown rate. While a clear correlation between spin behavior and superorbital phase has not been established in most systems, NGC 5907 ULX-1 did undergo an extended low-flux state lasting 3 yr, during which the pulsar exhibited significant spindown that can be interpreted as the propeller effect (F. Fürst et al. 2023). However, the 78 days superorbital modulation persists unchanged following the low-flux state, suggesting that regular superorbital modulation is not primarily driven by variations in the mass accretion rate, although intermittent off-states may still occur. Another example is NGC 300 ULX-1, a transient pulsating ULX that entered an extended low state in 2019, during which it continued to spin up (G. Vasilopoulos et al. 2019). This suggests that the mass accretion rate remained stable despite the drop in observed flux.

At the same time, the radiation-driven disk-warping model (J. E. Pringle 1996; G. I. Ogilvie & G. Dubus 2001) for superorbital modulation in SMC X-1 was also challenged with a few observational results. For example, P. Pradhan et al. (2020) claimed the detection of the pulsation during the low state, along with variations in the power-law spectral shape and normalization correlated with flux. This suggests that the flux changes may be, at least in part, intrinsic rather than solely due to obscuration or absorption. Moreover, the observed increase in the low-state flux and the lack of variability in the high-state flux during superorbital excursions are not fully consistent with the radiation-driven warped-disk model (C.-P. Hu et al. 2019). This does not rule out the disk warping but suggests that the warp inclination may have no connection to the radiation strength.

To probe whether the mass accretion rate varies across the superorbital cycle, the spin period evolution serves as a valuable proxy. SMC X-1 exhibits a long-term spinup trend, indicating a persistent accretion torque acting on the NS (S. Ínam et al. 2010; C.-P. Hu et al. 2019). However, detailed measurements of $\dot{\nu}$ within a single superorbital cycle have not yet been performed. Such analysis is challenging, due to the difficulty of obtaining long-term, high-cadence observations from large X-ray observatories. All-sky monitors like the Monitor of All-sky X-ray Image (MAXI) are suitable for studying long-term spin-frequency evolution (e.g., C.-P. Hu et al. 2019), but their short exposures per orbit (typically a few tens to hundreds of seconds) limit their ability to trace evolution within a single superorbital cycle. With the increasing feasibility of CubeSat technology, such observational campaigns have become practical. In this study, we utilize NinjaSat—a 6U CubeSat—to monitor the spin period evolution, flux variability, and spectral behavior of SMC X-1 during a superorbital high state.

2. Instrument Design and Observation

2.1. NinjaSat Observation and Data Reduction

NinjaSat is a nonimaging 6U CubeSat X-ray observatory with dimensions of 112.7 × 237.1 × 340.5 mm and a mass of 8 kg (T. Tamagawa et al. 2025). Launched in 2023, it provides continuous observations of bright X-ray sources and rapid response capabilities for transient follow-up. Equipped with two Gas Multiplier Counters (GMCs), NinjaSat offers a combined effective area of approximately 32 cm^2 at 6 keV, covering the 2–50 keV energy range with a temporal resolution of 61 μs. This submillisecond timing accuracy has been verified through observations of the Crab pulsar, by comparing the X-ray pulse profile with the radio ephemeris provided by the Jodrell Bank Observatory (A. G. Lyne et al. 2015; N. Ota et al. 2025; T. Tamagawa et al. 2025). A star-tracker-guided three-axis attitude control system enables fast and accurate pointing ($<0.^{\circ}1$), while onboard radiation-belt monitors ensure the safe operation of high-voltage components. This compact but powerful design allows NinjaSat to fill the observational gap between all-sky monitors and large X-ray observatories, enabling high-cadence, high-time-resolution data for both time- and frequency-domain studies.

We carried out two observation campaigns using NinjaSat. The first run took place from 2024 July 13 to August 11, as a test observation. It did not cover a complete high state of a superorbital cycle, and several large data gaps severely limited our ability to track the spin-frequency evolution in detail. To address this, a second campaign with a total ***net*** exposure of 331 ks across 485 pointings was carried out from 2024 December 13 to 2025 January 23, aimed at capturing the full superorbital ascending–high–descending phases. Although a few data gaps remained, the overall data quality was sufficient to study both the spectral variability and spin-frequency evolution across the superorbital cycle.

Throughout the entire campaign, only one GMC (GMC1) was in operation. Data reduction was performed with HEASoft version 6.33.1. Photon arrival times were corrected to the barycenter of the solar system using the `barycen` tool with the DE-405 ephemeris. To verify the detector energy calibration, NinjaSat regularly observes the Crab Nebula and several blank-sky fields. For the analysis of SMC X-1, we used background data from a blank-sky field at (R.A., decl.) = ($138.^{\circ}00$, $15.^{\circ}00$), known as BKGD_RXTE3 (K. Jahoda et al. 2006; R. A. Remillard et al. 2022), observed between 2024 November 15 and 2024 November 27, prior to the second monitoring campaign of SMC X-1. This 12 days observation provides the most statistically robust background data in the vicinity of the SMC X-1 monitoring period, with a total exposure of 114 ks.

The GMC has two readout pads: a circular inner electrode and an annular outer electrode. Following the event-selection criterion of T. Takeda et al. (2025), we extracted cleaned events from the inner electrode, to ensure a higher signal-to-noise ratio in the 2–20 keV energy range, further dividing them into soft (2–10 keV) and hard (10–20 keV) bands for analysis. We then corrected the X-ray reduction rate due to the passive collimator of the GMC, taking into account slight misalignments between its optical axis and the source direction, as well as attitude fluctuations during each observation. The average correction factor over the observation campaign was 1.14, given the collimator's field of view of $2.^{\circ}1$ at FWHM. Furthermore, for spectral analysis, we corrected the detector response of GMC1, following A. Aoyama et al. (2025), whose observations were carried out shortly before the current SMC X-1 and background observations. A uniform correction factor of 0.83 was applied to the effective area of GMC 1 across the

entire energy range, in addition to the collimator correction described above.

2.2. All-sky Monitoring Data

To ensure consistency between the NinjaSat results and the long-term spin period evolution, and to schedule the NinjaSat observations, we used both the Burst Alert Telescope (BAT) on board the Neil Gehrels Swift Telescope (Swift) and MAXI data to track the long-term flux variability. In addition, the long-term spin period evolution was derived from MAXI source event data.

2.2.1. MAXI

MAXI is a Japanese Experimental Module on board the International Space Station, equipped with two cameras: the Solid-state Slit Camera, with a collecting area of 200 cm^2, covering the energy range of 0.5–12 keV, and the Gas Slit Camera (GSC), with a collecting area of 5350 cm^2, covering 2–30 keV (M. Matsuoka et al. 2009). The monitoring light curve of SMC X-1,[11] obtained from the GSC and provided by RIKEN, JAXA, and the MAXI team, was extracted in the 2–20 keV energy band. The spectral hardness information was also available, as the light curves are divided into 2–4, 4–10, and 10–20 keV bands. We used the 1 day binned light curve to calibrate the flux scaling between Swift/BAT and MAXI/GSC, and we employed the 6 hr binned light curve for subsequent analysis.

In addition to the all-sky monitoring data, we extracted source events following the procedure described in C.-P. Hu et al. (2019). Photon events collected by the GSC, which provides a high time resolution of 50 μs (T. Mihara et al. 2011), were used for pulsation searches. We used 2–20 keV photons collected by GSC units 0, 1, 2, 4, 5, 7, and 8, because other GSCs were out of function (T. Mihara et al. 2011; M. Sugizaki et al. 2011). In this work, we present the pulse frequency evolution from MJD 60320 to MJD 60730, covering nine superorbital cycles. The source photons were extracted from a circular region with a radius of 1° centered on SMC X-1, ensuring the selection of $\gtrsim$90% of the source photons (T. Mihara et al. 2011).

2.2.2. Swift/BAT

The BAT on board Swift is designed primarily to detect gamma-ray bursts, with a large collecting area of 5200 cm^2. Since 2004, it has also been used to monitor known X-ray sources in the hard-X-ray band (15–150 keV), by scanning the entire sky approximately every 96 minutes (S. D. Barthelmy et al. 2005). In this study, we used the 15–50 keV light curve provided by the hard-X-ray transient monitor program[12] (H. A. Krimm et al. 2013).

Since MJD 59170, MAXI observations have intermittently experienced interruptions, due to occultations by the SpaceX Crew Dragon. We used the Swift/BAT light curve to fill these observational gaps. To align the datasets, we derive a linear scaling factor between the 1 day binned MAXI/GSC and Swift/BAT light curves and convert the BAT count rates into equivalent MAXI count rates.

[11] http://maxi.riken.jp/star_data/J0117-734/J0117-734.html
[12] https://swift.gsfc.nasa.gov/results/transients/SMCX-1/

3. Results

3.1. NinjaSat Light Curve of 2024 December Campaign

We first generated the NinjaSat light curve using 1 s time bins and applied collimator corrections as described in Section 2.1. Then, the light curve was rebinned over each Good Time Interval (GTI), with exposure times ranging from approximately 50 to 1000 s. To guarantee a sufficient signal-to-noise ratio, we excluded GTIs with effective exposure times shorter than 200 s.

The resulting 2–20 keV light curve is shown in Figure 1(a), with the count rate converted to units of mCrab. This conversion was performed by dividing the background-subtracted count rates (0.247 counts s^{-1} for the 2–10 keV background and 0.148 counts s^{-1} for the 10–20 keV background) by the corresponding Crab count rates (10.29 counts s^{-1} for 2–10 keV and 1.039 counts s^{-1} for 10–20 keV). For comparison, the 6 hr binned MAXI light curve and the scaled 1 day binned Swift/BAT light curve are also shown. In the subsequent timing analysis, we excluded data collected during orbital eclipses (highlighted in green in Figure 1(a)), defined as orbital phases between 0.9 and 1.1, based on the orbital ephemeris from C.-P. Hu et al. 2019.

Figure 1 also highlights the superorbital transition states: ascending, defined as $\phi_{\rm sup} = 0.0$–0.1, and descending, defined as $\phi_{\rm sup} = 0.65$–0.8, are indicated with a light gray background. The superorbital low state is marked with a dark gray background. A total of 11 orbital cycles were observed by NinjaSat, where the out-of-eclipse intervals are labeled as "i" through "xi."

The hardness ratio, defined as the 10–20 keV flux divided by the 2–10 keV flux, for noneclipse GTIs is shown in Figure 1(b). The ratio remains largely stable, even during the superorbital ascending and descending states, except for preeclipse dips observed during the descending state (around MJD 60692 and MJD 60696). This suggests that absorption is unlikely to be the dominant factor in superorbital flux variability.

The NinjaSat observation covered 41 days, from MJD 60657 to MJD 60698. Although it did not cover the full superorbital cycle, it captured the complete ascending–high–descending sequence and part of the low state, corresponding to a superorbital phase range of $\phi_{\rm sup} = 0$–0.87. For this campaign, the start of the superorbital cycle is defined as MJD 60657.5, marking the onset of the rising edge. The end of the cycle was not captured by either NinjaSat or MAXI but is evident in the Swift/BAT light curve, occurring at MJD 60704.5.

This results in a superorbital cycle duration of 47 days, which is clearly shorter than the average cycle length during non-excursion epochs (approximately 53–57 days) but close to those observed during excursion epochs (typically 45–46 days; see C.-P. Hu et al. 2019, 2023). Thus, this cycle likely represents a mini excursion, a phenomenon occasionally observed during regular epochs and lasting for one to four cycles.

3.2. NinjaSat Pulsar Timing

Our goal is to perform phase-connected (coherent) or semicoherent time-of-arrival (TOA) analysis to track the spin period evolution in detail. As a preliminary step, we collected photons within each binary orbital period and performed a two-dimensional Z_2^2-test to search for both the spin frequency ν and its derivative $\dot{\nu}$ (R. Buccheri et al. 1983).

To correct for orbital Doppler effects, we used a binary orbital ephemeris with a mideclipse time of $T_{\rm mid\text{-}eclipse} =$ MJD 60505.7361918, an orbital frequency of $f_{\rm orb} = 0.25696017$ day^{-1}, and a frequency derivative of $\dot{f}_{\rm orb} = 2.379 \times 10^{-9}$

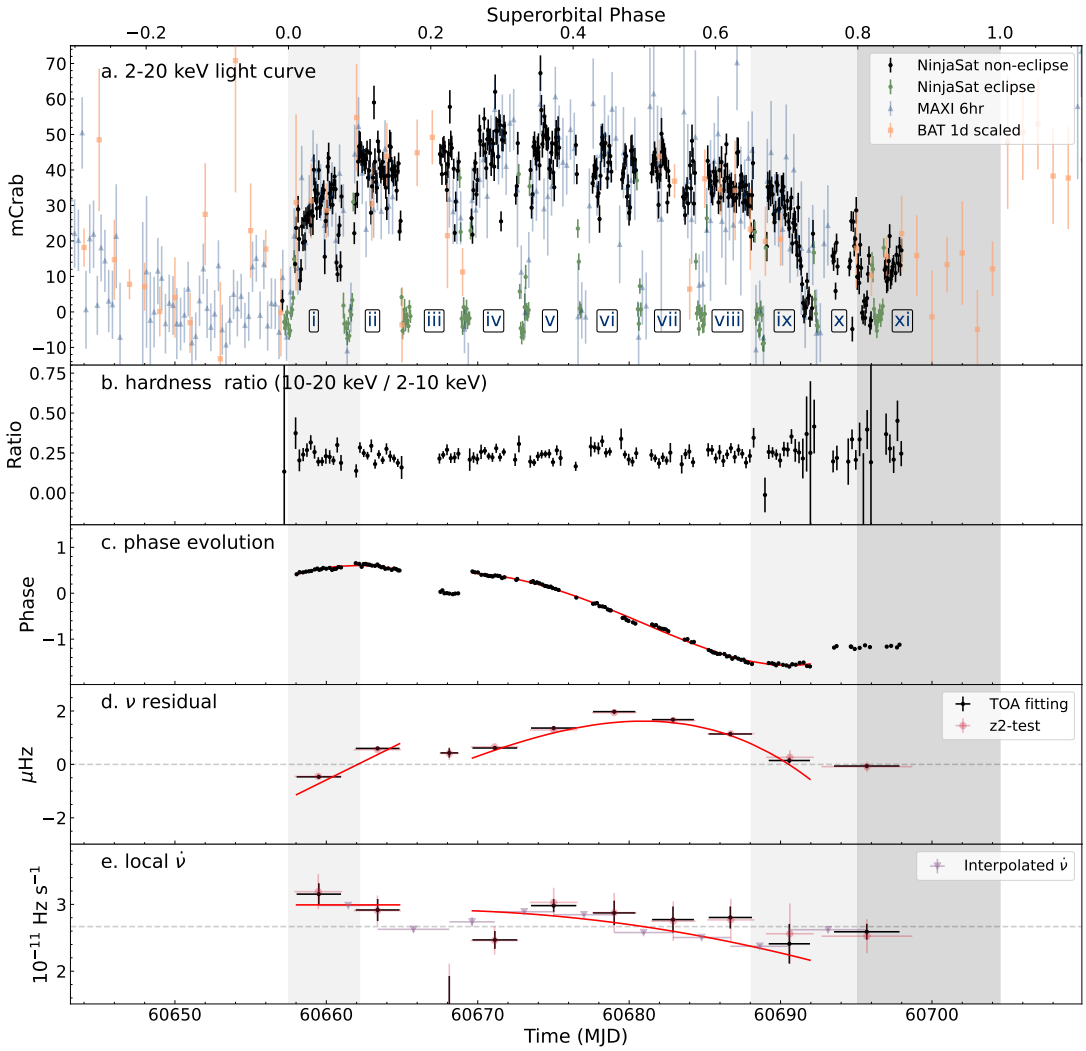

Figure 1. (a). Light curve of SMC X-1 obtained with NinjaSat (black dots), MAXI (green triangles), and Swift/BAT (orange squares). NinjaSat data collected during orbital eclipses are shown in green. The light gray shaded regions indicate the superorbital ascending (MJD 60657–60662) and descending (MJD 60688–60695) states, while the dark gray region marks the superorbital low state (MJD 60695–60704). 11 observed orbital cycles are labeled "i" to "xi." (b). Hardness ratio (10–20 keV/2–10 keV) derived from NinjaSat observations. (c). Evolution of pulse arrival phases relative to a quadratic ephemeris with $\dot{\nu} = 2.668 \times 10^{-11}$ Hz s^{-1}, based on the average spinup rate during this superorbital cycle. The red curves denote the best-fit quadratic (cycles i to ii) and fourth-order polynomials (cycles iv to ix). (d). Spin period deviations relative to the quadratic model. The spin periods for each orbital cycle are derived from TOA fitting (black points) and cross-validated using the Z_2^2-test (orange diamonds). (e). Evolution of the local $\dot{\nu}$. The red curves in panels (d) and (e) are derived from the timing solutions in panel (c).

day^{-2}. The $f_{\rm orb}$ and $\dot{f}_{\rm orb}$ are based on C.-P. Hu et al. (2019), with the mideclipse time shifted to match the epoch of the NinjaSat observation. Additionally, we found that TOAs within a single orbital cycle exhibited residual modulation on the timescale of the orbital period, which was reduced by shifting $T_{\rm mid\text{-}eclipse}$ by 100 s. This adjustment allows the ephemeris to effectively correct for orbital Doppler effects across the NinjaSat observation window.

After determining the local ν and $\dot{\nu}$, we divided the binary orbit into multiple segments. Each segment contains two to six NinjaSat orbits and collected approximately 2000–3000 photons. We then calculated the TOA for each segment using the unbinned maximum-likelihood method (M. A. Livingstone et al. 2009). The phase of each TOA was computed using a long-term average spin frequency of $\nu = 1.4362513237$ Hz and a spinup rate of $\dot{\nu} = 2.6676 \times 10^{-11}$ Hz s^{-1} obtained from the NinjaSat campaign. The resulting TOA phase evolution is shown in Figure 1(c).

To estimate the local values of ν and $\dot{\nu}$, we fit the TOA phases with a second-order polynomial and present the results in Figures 1(d) and (e), respectively. For comparison, spin parameters derived from the local Z_2^2-test are also plotted, to verify consistency. Finally, we also estimated the average spinup rate by calculating the change in ν between consecutive measurements divided by the elapsed time.

From the TOA phase evolution, we identified a possible phase discontinuity around MJD 60670, where the phase exhibits a jump of approximately 0.4 cycles, following the orbital eclipse of cycle iii. Unfortunately, the first half of orbital cycle iii was not covered by NinjaSat, making it difficult to constrain $\dot{\nu}$ precisely across this interval. To account for the discontinuity, we divided the TOA phase evolution into two segments—MJD 60658–60662 and MJD 60670–60692—and fit each segment with high-order polynomials (Figure 1(c)). Taking the time derivative of the best-fit phase models, we derived the predicted evolution of ν and $\dot{\nu}$ (Figures 1(d) and (e)). These

model-predicted trends are consistent with the local ν and $\dot{\nu}$ values obtained from piecewise TOA fitting and the Z_2^2-test results.

Both analyses suggest that the local $\dot{\nu}$ during orbital cycle iii appears to drop sharply, although the associated uncertainty is relatively large. Following this cycle, a significant and abrupt increase in flux is observed, accompanied by a rise in $\dot{\nu}$, suggesting that the spinup rate may be sensitive to changes in flux.

Another discontinuity is detected during the late descending phase, around MJD 60694, near the end of the orbital cycle x. This may be attributed either to flux variability or to the contamination of reflection components from the innermost regions of the accretion disk.

3.3. Pulse Profile Evolution

To investigate the pulse profile variability, we folded the light curve within each orbital cycle using the corresponding local ν and $\dot{\nu}$ values. Of the 11 orbits observed with NinjaSat, cycles iii and xi were only partially covered, due to technical issues and scheduling constraints. Additionally, several orbits, including iv, v, vi, vii, and x, contained significant data gaps. Nevertheless, we successfully derived the 2–20 keV pulse profiles for each orbit, which are presented in Figure 2.

All pulse profiles exhibit a double-peaked structure, consisting of a narrower peak (P1) spanning approximately 0.45 cycles and a broader peak (P2) spanning about 0.55 cycles. At the beginning of the superorbital cycle, P1 has a lower amplitude than P2, but its amplitude gradually increases with superorbital phase. The two peaks reach similar amplitudes at $\phi_{\rm sup} \approx 0.25$–$0.35$. Beyond $\phi_{\rm sup} \approx 0.35$, P1 becomes more prominent than P2, peaks in relative strength around $\phi_{\rm sup} \approx 0.5$, and then begins to decline. Pulsations remain detectable at $\phi_{\rm sup} \approx 0.85$–$0.87$, and the pulse profile in this phase range resembles that observed at $\phi_{\rm sup} \approx 0.02$–$0.09$, though with greater uncertainties due to limited photon statistics.

This pulse profile behavior is consistent with the findings of P. Pradhan et al. (2020), and the continuous monitoring by NinjaSat enables us to trace its evolution within a single superorbital cycle. To parameterize the pulse profile, we define the pulse fraction (PF) of P1 as $\mathrm{PF1} = (P_{\rm max,1} - P_{\rm UP})/(P_{\rm max} + P_{\rm UP})$, where $P_{\rm max,1}$ is the averaged count rate over a 0.15 cycle interval centered on the peak of P1, $P_{\rm UP}$ is the mean count rate over $\phi_{\rm spin} = 0.95$–1.05 and 0.4–0.5, and $P_{\rm max}$ is the peak count rate of the entire spin cycle, which equals $P_{\rm max,1}$, if P1 is stronger than P2, or $P_{\rm max,2}$, otherwise. Similarly, the PF of P2 is given by $\mathrm{PF2} = (P_{\rm max,2} - P_{\rm UP})/(P_{\rm max,2} + P_{\rm UP})$. To characterize the relative strengths of these two peaks, we define the peak ratio as $\mathrm{peakratio} = \mathrm{PF2}/\mathrm{PF1} = (P_{\rm max,2} - P_{\rm UP})/(P_{\rm max,1} - P_{\rm UP})$. Due to limited photon statistics, the parameters in orbital cycles x and xi were poorly constrained. Therefore, we carried out correlation analysis on orbital cycles i to ix only.

Figure 3 shows the flux dependence of PF1, PF2, and the peak ratio. The peak ratio ranged from approximately 0.9 to 1.6 during the NinjaSat campaign. Meanwhile, PF1 showed slightly lower values (0.3–0.45) compared to PF2 (0.35–0.5). A negative correlation is found between the flux and peak ratio, with a Pearson coefficient of $\rho = -0.84$ and a p-value of $p = 0.004$, corresponding to a $\approx 3\sigma$ significance level. The correlation between the flux and PF1 is marginally positive ($\rho = 0.75$, $p = 0.02$), whereas the flux and PF2 show a relatively weaker anticorrelation ($\rho = -0.66$, $p = 0.05$).

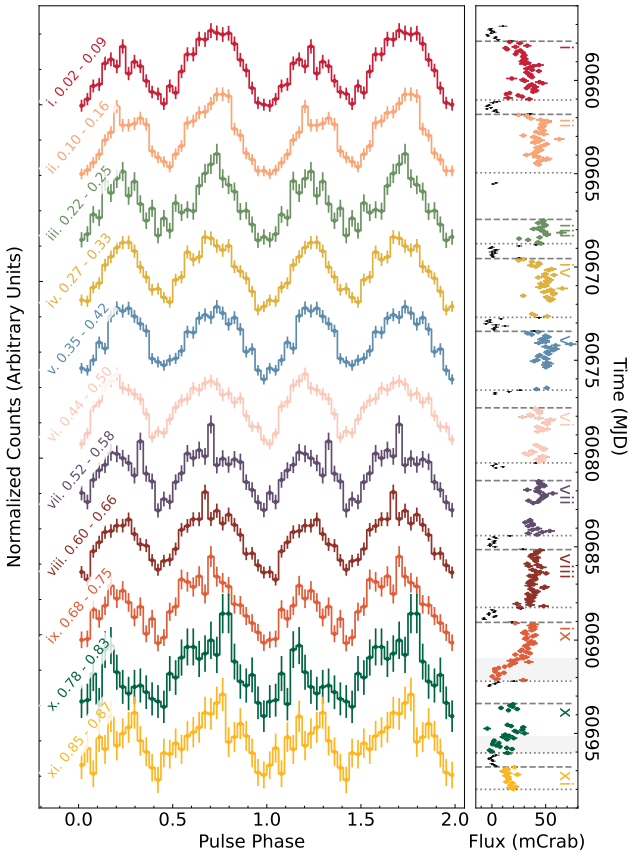

Figure 2. Pulse profile evolution of SMC X-1 observed with NinjaSat. Pulse profiles for 11 orbital cycles (i to xi) are shown sequentially and color-coded, with their corresponding superorbital phase ranges labeled. Photon events from orbital eclipses and preeclipse dips were excluded from the folded light curves. The right panel displays the NinjaSat light curve. The black dots indicate data during orbital eclipses, while out-of-eclipse points are color-coded according to orbital cycle. The dotted lines mark the boundaries of the out-of-eclipse intervals for each orbital cycle. Preeclipse dips in cycles ix and x are marked by the gray filled regions. The photons collected during these intervals were excluded from the pulse profiles.

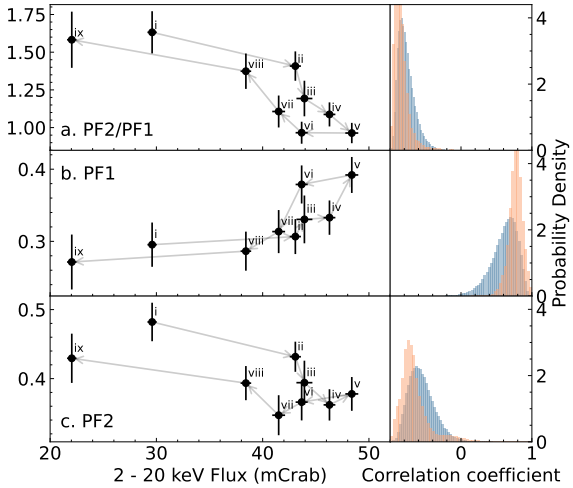

Figure 3. Flux dependence of the peak ratio (a), PF of P1 (b), and PF of P2 (c). The gray arrows indicate the evolutionary track of each parameter from orbital cycle i through ix. The right panels show probability density distributions from Monte Carlo simulations (blue) and bootstrapped samples (orange).

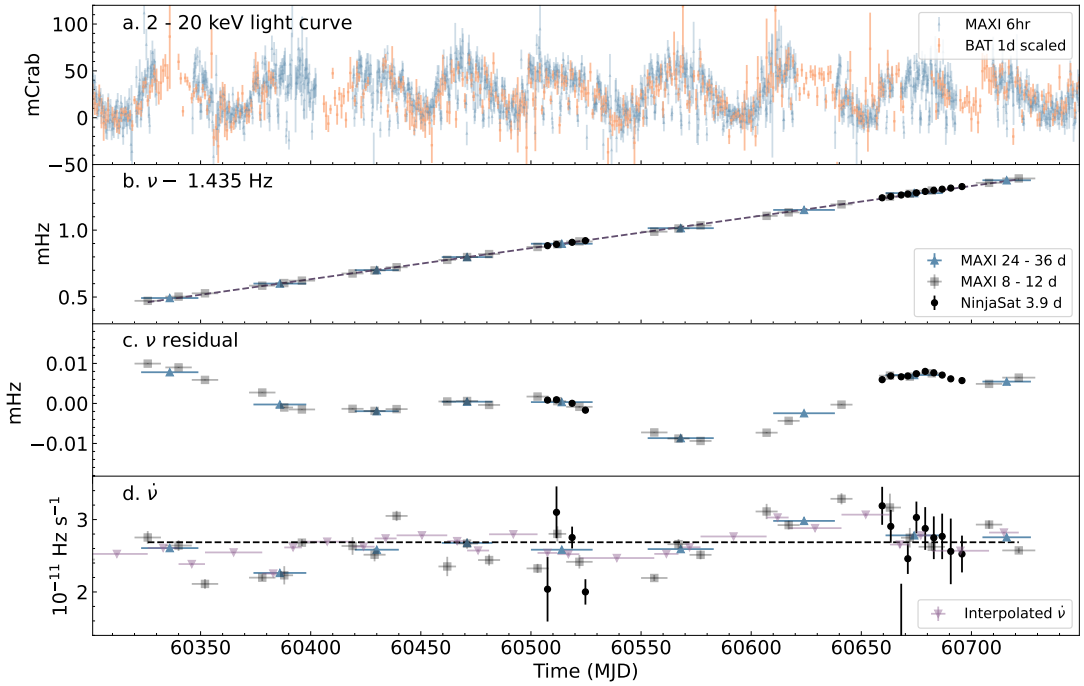

Figure 4. Long-term spin evolution of SMC X-1 observed with NinjaSat and MAXI. (a). The 2–20 keV MAXI 6 hr binned light curve is plotted in blue, and the scaled 1 day binned Swift/BAT light curve is plotted in orange. (b). Spin-frequency (ν) evolution. The blue triangles represent values averaged over individual superorbital high states using MAXI data; the gray squares show values computed over 8–12 days intervals; and the black dots indicate NinjaSat measurements for each binary orbital cycle. The black dashed line is a linear fit to the 8–12 days MAXI ν measurements. (c). Residuals of ν after subtracting the best-fit linear trend shown in panel (b). (d). Evolution of the spinup rate ($\dot{\nu}$). The dashed line represents the best-fit average $\dot{\nu}$ across the nine superorbital cycles, as determined from the linear model in panel (b).

To further evaluate the influence of uncertainties and potential outliers, we performed both Monte Carlo and bootstrap simulations. For the Monte Carlo simulations, we generated simulated samples, by assuming the uncertainties in the flux and peak ratio as the diagonal elements of a bivariate Gaussian covariance matrix. For the bootstrap analysis, we randomly resampled the dataset with replacement, keeping the sample size constant. After 10^5 simulations for each method, the resulting distributions of ρ are shown in the right panel of Figure 3.

In the case of the flux-versus-peak ratio, only five Monte Carlo samples and 91 bootstrap samples exhibited positive correlation coefficients, supporting a statistically significant negative correlation. For the correlation between the flux and PF1, 533 Monte Carlo samples and 48 bootstrap samples had $\rho < 0$, suggesting a moderate positive correlation when measurement uncertainty is taken into account. Finally, in the flux–PF2 correlation, 580 Monte Carlo and 2374 bootstrap samples yielded positive ρ, indicating a marginal significant negative correlation. We also tested the impact of energy selection by increasing the lower bound of energy selection, producing pulse profiles in the 3–20 and 4–20 keV bands. The positive correlations between PF1 and flux, as well as between the peak ratio and flux, remain prominent. In contrast, PF2 shows only a weak positive correlation with flux. These results imply that the broader peak remains relatively stable with flux or follows a more nonlinear relationship than a simple trend. In contrast, the narrower peak shows clear variability linked to the superorbital phase.

We further investigated the mean hardness ratio variability of both pulse peaks and found no significant flux dependences across the superorbital cycle. For P1, the result is $\rho = 0.45$ ($p = 0.22$), and for P2, it is $\rho = -0.44$($p = 0.24$), indicating no statistically significant correlation.

3.4. Long-term Spin-frequency Evolution

The NinjaSat observations suggest that the $\dot{\nu}$ may be flux-dependent. To investigate whether this behavior is part of a longer-term trend, we analyzed MAXI photon event data and searched for ν and $\dot{\nu}$ over 8–12 days intervals, based on photon statistics. For comparison, we also calculated average values of ν and $\dot{\nu}$ for each superorbital cycle. In addition to the MAXI data, we analyzed another NinjaSat dataset from a test observation campaign carried out in 2024 July–August, which spanned approximately 20 days. Similar to the December campaign, we derived ν and $\dot{\nu}$ for individual orbits, resulting in four additional data points.

The long-term evolutions of ν and $\dot{\nu}$ are shown in Figure 4. We present the spin-frequency evolution over nine superorbital cycles, covering the interval from MJD 60330 to 60730. Figure 4(b) displays the spin frequency, which exhibits a steady spinup trend. Fitting this trend with a linear model yields an average spinup rate of $\dot{\nu} = 2.69(1) \times 10^{-11}$ Hz s^{-1}. After subtracting this long-term trend, the residuals are shown in Figure 4(c), revealing modulation with a timescale of roughly four superorbital cycles.

Figure 4(d) shows the evolution of $\dot{\nu}$, which also displays clear modulation. Notably, the variations in $\dot{\nu}$ are more abrupt and exhibit greater fluctuations compared to the smoother residuals in ν. Additionally, the $\dot{\nu}$ modulation seems to lead the ν residuals by approximately one superorbital cycle. To fill in data gaps caused by missing data and superorbital low states, and to check the consistency of the spin evolution, we also estimated the interpolated spinup rate from the ν measured with MAXI.

From the long-term evolution, it is clear that the superorbital cycle observed during the December campaign lies on a

plateau in the ν residual plot, coinciding with a declining trend in the long-term $\dot{\nu}$ across neighboring superorbital cycles. This suggests that the apparent drop in frequency residual during the ascending and descending phases of the December campaign is likely coincidental, rather than an intrinsic dependence on superorbital phase.

3.5. Spectral Evolution

We used NinjaSat to perform spectral analysis over this superorbital cycle. Orbital cycles i, ii, iv, viii, and ix were nearly continuously monitored. This allows us to divide their noneclipse phases into two time segments each. Most importantly, the second half of orbital cycle ix likely corresponds to a preeclipse dip, enabling a comparison between regular and dip spectra. Other orbital cycles contain significant data gaps, so they were not subdivided for spectral analysis. This resulted in a total of 16 time segments used for spectral analysis.

We performed all spectral analyses using XSPEC version 12.14.0. The absorption model `tbabs` was adopted, with interstellar abundances set according to J. Wilms et al. (2000), in which the cross sections were adopted from D. A. Verner et al. (1993). We grouped the spectra, to ensure that each spectral bin contained at least five photons, and used Cash statistics for spectral fitting (W. Cash 1979).

The X-ray spectrum of SMC X-1 is typically described with a blackbody component, a power law with a high-energy cutoff, and several emission lines. The power-law continuum is commonly modeled using cutoffpl (e.g., P. Pradhan et al. 2020; R. Karam et al. 2025) or `highecut*powerlaw` (e.g., J. Neilsen et al. 2004; R. C. Hickox & S. D. Vrtilek 2005). Prominent spectral lines often include Fe Kα, Ne X Lyα, Ne IX, and O VIII Lyα (M. C. Brumback et al. 2020). However, these line features are not detectable in the NinjaSat data, due to the limited effective area and the low energy resolution of the gas detector. Therefore, we tested two continuum models: `tbabs*pcfabs*cutoffpl` and `tbabs*pcfabs*highecut*powerlaw`. In both models, `pcfabs` is used to represent partial covering by the warped accretion disk. The blackbody component is not included, because its contribution is negligible above 2 keV.

We fit all 16 spectra simultaneously. The hydrogen column density ($N_{\rm H}$) in the `tbabs` model was frozen at 2.5×10^{21} cm^{-2} (R. Karam et al. 2025), while the $N_{\rm H}$ of the `pcfabs` component was a free parameter. The e-folding energy in the `cutoffpl` model cannot be constrained for individual datasets. Therefore, it was linked across all datasets. This model yielded a total fit statistic of 2713.16 with 2783 degrees of freedom, corresponding to a null-hypothesis probability of 0.29. On the other hand, the `highecut*powerlaw` model presented difficulty in simultaneously constraining the cutoff energy (E_c) and e-folding energy (E_f), so we linked these two parameters across all datasets. This resulted in a total fit statistic of 2717.28 with 2797 degrees of freedom and a higher null-hypothesis probability of 0.27. Both models are statistically acceptable. Therefore, we adopt the `tbabs*pcfabs*cutoffpl` model, with the e-folding energy of exponential rolloff $E_f = 3.2^{+0.4}_{-0.5}$ keV linked across all datasets, for reporting the spectral evolution.

The spectral parameter evolution is shown in Figure 5. The column density ($N_{\rm H}$) derived from the pcfabs component is generally large and poorly constrained. High covering fractions exceeding 0.9 are found in the superorbital low state,

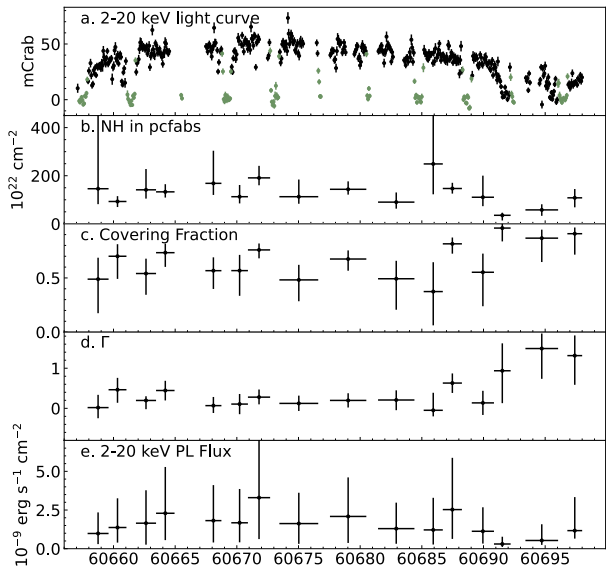

Figure 5. Spectral evolution of SMC X-1 during the NinjaSat monitoring campaign from 2024 December to 2025 January. (a) The 2–20 keV light curve is presented as a reference. (b)–(e) The corresponding evolution of spectral parameters derived from the best-fit pcfabs*cutoffpl model: (b) $N_{\rm H}$ from the pcfabs component; (c) partial covering fraction; (d) photon index (Γ); and (e) unabsorbed flux (2–20 keV band).

including two preeclipse dips. The photon index Γ and PL flux show no strong dependence on superorbital phase, except during the low states. In addition, the Γ is frequently found between 0 and 1, occasionally approaching zero. These are partially consistent with those reported by K. C. Dage et al. (2022) and R. Karam et al. (2025), though with significantly larger uncertainties. The increased uncertainty may arise from parameter degeneracy between the partial covering $N_{\rm H}$ in `pcfabs` and Γ, likely due to the limited soft-X-ray sensitivity ($<$2 keV) and photon statistics of NinjaSat for dealing with complex spectral models. Therefore, although a softer spectrum is suggested in the low state, the larger uncertainties make this inconclusive. These findings indicate that the spectral shape remains broadly stable throughout the superorbital cycle in the NinjaSat energy range.

To illustrate the spectral variability of SMC X-1 and demonstrate the observational capabilities of NinjaSat, we present three representative spectra in Figure 6. They represent different superorbital states: the ascending state (first half of orbit i), the high state (second half of orbit iv), and the low state (first half of orbit xi). They correspond to the first, seventh, and last data points in Figure 5.

4. Discussion

With the NinjaSat observations, we have successfully traced the spin-frequency evolution of SMC X-1 across a superorbital cycle lasting just 47 days, which indicates a mini excursion. We found that while the spinup rate varies, this variability appears to be governed by longer-term trends, rather than being directly tied to the superorbital phase. Despite significant X-ray flux variations between approximately 10 and 50 mCrab, the hardness ratio remains relatively stable, between 0.2 and 0.3, with slight increases observed only during preeclipse dips. The flux during the superorbital low state in the cycle between MJD 60650 and 60700 is approximately 10–20

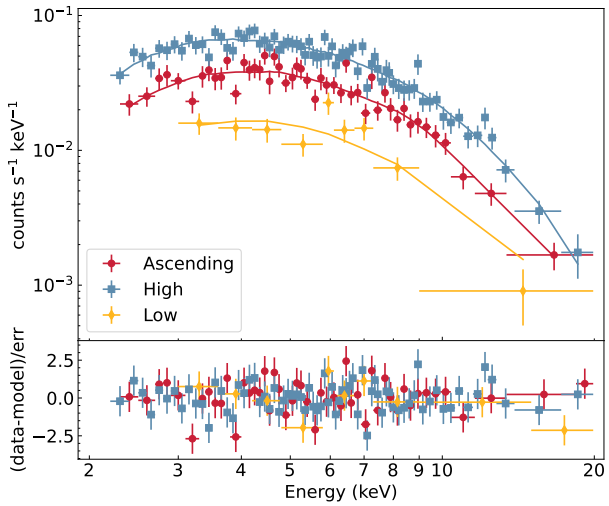

Figure 6. Three example spectra observed with NinjaSat. The spectrum during the ascending state corresponds to the first data point in Figure 5; the high-state spectrum is taken from the seventh point; and the low-state spectrum is from the last data point. The bottom panel displays residuals normalized to data uncertainties. Spectra are rebinned for display, to maintain a signal-to-noise ratio above 5 for display purposes.

mCrab, higher than in typical low states during regular epochs. Pulsations remain detectable even during this low state, and we observed clear evolution in the pulse profile as a function of superorbital phase. All the spectra can be described with a cutoff power law, where the partial covering fraction increased to higher than 90% during the preeclipse dips and superorbital low state. These observational results provide hints at the nature of superorbital modulation, the interaction between the magnetosphere and the inner accretion disk, and the geometry of the disk itself. We explore the implications of these findings in the following discussion.

First, although the spinup rate of SMC X-1 is variable, the spin frequency increases monotonically throughout the observation period. This indicates that the magnetospheric radius ($r_{\rm m}$), which is believed to be the innermost radius of the accretion disk, remains well within the corotation radius ($r_{\rm co}$). Under this condition, the spinup rate is expected to be proportional to the mass accretion rate ($\dot{m}$). Following L. Bildsten et al. (1997), the relationship can be expressed as

$$\dot{\nu} \approx 1.6 \times 10^{-13}{\rm s}^{-2}\left(\frac{\dot{m}}{10^{-10}M_{\odot}{\rm yr}^{-1}}\right) \times\left(\frac{\nu}{\rm Hz}\right)^{-\frac{1}{3}}\left(\frac{r_{\rm m}}{r_{\rm co}}\right)^{\frac{1}{2}}. \quad (1)$$

Assuming standard magnetospheric accretion, the luminosity is also proportional to $\dot{m}$, implying that $\dot{\nu}$ should also be proportional to the luminosity. In our observations, the X-ray flux varies by at least a factor of 5. However, the measured change in spinup rate between high and low states is only about 13(5)% if we compare orbital cycles v and x–xi. This discrepancy suggests that the superorbital modulation is primarily due to geometric effects rather than intrinsic changes in the accretion rate.

This can be further examined through a correlation analysis between the flux and $\dot{\nu}$ (see Figure 7). The Pearson correlation coefficient ($\rho = -0.1$, $p = 0.76$), supported by results from the Monte Carlo and bootstrap methods, indicates no statistically

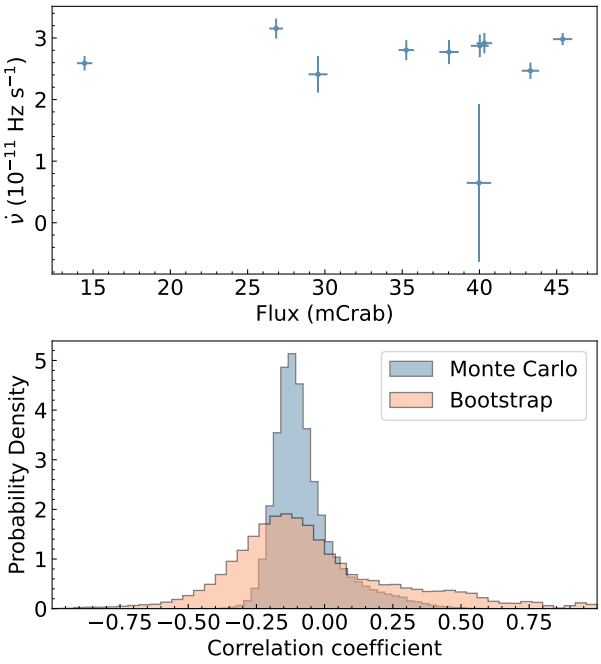

Figure 7. Correlation between $\dot{\nu}$ and 2–20 keV flux. No statistically significant correlation was observed from either Monte Carlo simulations or bootstrap resampling.

significant correlation. The lack of correlation implies that $\dot{\nu}$ is not directly related to the observed flux, supporting the interpretation that superorbital modulation is not primarily driven by changes in the mass accretion rate.

In addition, an intriguing phase discontinuity is observed between orbital cycles iii and v. We observed a ≈10% increase in $\dot{\nu}$ across these orbital cycles, confirmed by both direct and interpolated measurements (Figure 1(e)). This event aligns with a ≈10% increase in X-ray flux (Figure 3). This coincidence suggests a potential short-term link between the flux and spinup rate during the superorbital high state, where the covering fraction is relatively stable. A similar discontinuity occurs between cycles ix and xi, but strong flux variations due to superorbital modulation and preeclipse dips prevent further interpretation.

Since the superorbital modulation is unlikely to be primarily driven by mass-accretion-rate change, the warped-accretion-disk model remains one of the most plausible explanations. However, this model also faces certain challenges. One key issue is the lack of significant spectral or hardness ratio variability across the superorbital cycle, except during preeclipse dips. Although previous studies have suggested spectral hardening in the superorbital low state, such hardening has only been observed during the deepest low states and is associated with large uncertainties (S. Trowbridge et al. 2007; C.-P. Hu et al. 2019). Notably, no clear spectral hardening and spectral parameter change are seen during the superorbital transition phases. This suggests that the warped region of the accretion disk is highly opaque across the entire X-ray bands. The gradual flux changes observed during the superorbital transitions, as well as the variability within the low state, may instead be attributed to variations in the partial covering fraction. Recent spectral analyses with NICER have revealed an anticorrelation between the observed flux and partial covering fraction, supporting this interpretation (R. Karam et al. 2025).

If the superorbital modulation is indeed caused by partial obscuration from an opaque warped accretion disk, the inner disk must lie close enough to make the NS have a non-negligible angular size. The corotation radius, estimated from the NS spin frequency, is approximately 1300 km. In contrast, the inner disk radius may be much smaller. For instance, B. Paul et al. (2002) estimated an inner radius of 300–400 km, based on modeling of the soft spectral component, though this does not fully explain the detection of pulsations below approximately 2 keV. If this small inner radius is correct, the NS would have an angular size of roughly 4° as seen from the inner disk. This is sufficient for partial covering. Under this geometry, precession of the warped disk could produce gradual transitions between high states (NS fully visible) and low states (partially or mostly obscured). Furthermore, small variations in the disk structure could result in a shallower low state if the warp is flatter and fails to fully obscure the NS. While this scenario is plausible, understanding the link between short superorbital cycle lengths and the observed shallow low states remains crucial for a comprehensive understanding of this system.

Although the superorbital modulation is unlikely to be caused by changes in the mass accretion rate—i.e., not driven by the "propeller" effect—this does not rule out the possibility of a supercritical accretion scenario (see P. Kaaret et al. 2017 for a review). In this scenario, the inner accretion disk becomes geometrically thick, due to radiation pressure (A. R. King 2008). If the inner disk is asymmetric to the orbital plane and undergoes precession, it can (quasi)periodically obscure the X-ray emission from the NS, similar to the mechanism proposed in the radiation-driven warp model. In this scenario, optically thin material is likely blown away from the upper layer of the accretion disk, leaving behind an opaque structure. This could naturally explain the lack of significant spectral changes during the superorbital transitions, as the remaining disk materials are optically thick in the X-ray band. In addition, since the intrinsic luminosity of SMC X-1 is as high as 1.3×10^{39} erg s^{-1}, the inner accretion disk is likely to be highly ionized. Under these conditions, the observed decrease in flux during the low state can also be explained by nearly-energy-independent electron scattering, rather than increased absorption or spectral hardening. A similar mechanism is also expected in the precessing ring tube model (H. Inoue 2019). Finally, the ejected material is expected to form a funnel-shaped wind, driving ultrafast outflows at semirelativistic speeds, as seen in NGC 300 ULX-1 (P. Kosec et al. 2018). Such features may be detectable with future high-spectral-resolution X-ray missions like the X-Ray Imaging and Spectroscopy Mission.

The hard-X-ray ($\gtrsim$2 keV) pulse profile of SMC X-1 is generally characterized as double-peaked and stable across the superorbital phase. In contrast, the soft-X-ray component ($\lesssim$2 keV) shows significant variability. Their phase-dependent difference has long supported the warped-disk model (J. Neilsen et al. 2004; R. C. Hickox & S. D. Vrtilek 2005). However, variability in the hard-X-ray band has received limited discussion. Our NinjaSat observations confirm the result obtained in P. Pradhan et al. (2020) that the hard-X-ray pulse profile is modulated by superorbital phase, which is not dominated by intrinsic flux variability. If the NS is effectively a point source as seen from the inner accretion disk, geometric effects cannot account for the observed variability. On the other hand, if the NS has a nonnegligible angular size, the two pulsar beams may experience differing covering fractions, depending on the superorbital phase. Such a scenario has been successfully developed to explain the pulse profile variability in Her X-1 (D. M. Scott et al. 2000). Given that the pulse profile of SMC X-1 is quite different from that of Her X-1, and that no corresponding simulations have been performed, this hypothesis could be tested in future work, through detailed theoretical modeling and superorbital/pulse phase-resolved spectroscopy.

The precession of the NS spin axis presents a plausible alternative explanation for the pulse profile evolution, similar to the mechanism proposed for Her X-1 (R. Staubert et al. 2009, 2013). In the case of Her X-1, the precession of the NS is considered a more stable clock than the disk precession, with the two synchronized through a feedback mechanism. This coupling may weaken when the inner inclination of the accretion disk decreases. This scenario not only explains the pulse profile evolution within a superorbital cycle, but also accounts for correlations between spin period changes and the appearance of anomalous low states. X-ray polarization observations with the Imaging X-ray Polarimetry Explorer (IXPE) have provided evidence for the free precession of the NS in Her X-1 (V. Doroshenko et al. 2022; J. Heyl et al. 2024). A similar behavior is also observed in SMC X-1 (S. V. Forsblom et al. 2024). MAXI data reveal a spinup-rate acceleration before the most recent superorbital excursion (Figure 2 in C.-P. Hu et al. 2023), supporting an inside-out mechanism, where the NS behavior influences disk structure. However, this connection is not always observed. No such change in spin frequency was detected around the shorter 2014 excursion (C.-P. Hu et al. 2019, 2023). Future long-term monitoring will be crucial for testing the consistency between the pulse profile evolution and superorbital modulation. Finally, the hypothesis of NS spin-axis precession can also be independently tested using X-ray polarization with IXPE over the superorbital cycle.

5. Summary

In this work, we present the first high-cadence, long-term timing and spectral monitoring of SMC X-1 across nearly an entire superorbital cycle using NinjaSat. This unique observational campaign allowed us to continuously trace the spin frequency and spinup rate and enabled a direct test of whether the spin evolution correlates with the X-ray flux across different superorbital states. Combining NinjaSat and MAXI data, we find that the spinup rate during the high state remains consistent with the long-term average and shows no significant correlation with instantaneous flux, even during low and transitional states. This strongly suggests that the superorbital modulation is not driven by intrinsic changes in the mass accretion rate, but is instead geometric in origin, likely caused by obscuration from a precessing optically thick warped accretion disk or energy-independent electron scattering.

Our spectral analysis supports this interpretation. Both the hardness ratio and the overall spectral shape remain stable throughout the superorbital cycle, including the low states. This spectral stability implies that observed superorbital flux changes are not accompanied by changes in absorption of a neutral fully covering absorber, consistent with the partial covering scenario.

A possible short-term link between $\dot{\nu}$ and flux is observed in the high state, where both increased by approximately 10%. This result suggests that local flux variability could be caused by changes in the mass accretion rate. A longer-term trend (longer than a single superorbital cycle) is also observed in the combined NinjaSat and MAXI campaign, although further analysis is needed to test the connection between the flux and spinup rate over such timescales.

Finally, we detect superorbital-phase-dependent variations in the 2–20 keV pulse profile. These changes are primarily associated with variations in the PFs of the two peaks in the profile. This behavior could be interpreted by either the variability of the covering fraction of two hotspots or the precession of the NS spin axis. Continued long-term monitoring, detailed theoretical modeling, and polarization observation will be essential for testing the stability and origin of this pulse profile evolution.

Beyond these scientific insights, our study demonstrates the capability of CubeSats like NinjaSat for long-term, high-cadence observations of bright X-ray sources. Future CubeSat missions with better energy resolution, broader spectral coverage, or multiwavelength capability could greatly expand our understanding of accreting compact objects.

Acknowledgments

We thank the anonymous referee for valuable comments that improved this paper. This project was supported by the Japan Society for the Promotion of Science (JSPS) KAKENHI (JP17K18776, JP18H04584, JP20H04743, JP24K00673, and JP25KJ0241). C.-P.H. acknowledges support from the National Science and Technology Council in Taiwan through grant 112-2112-M-018-004-MY3 and from the JSPS Invitational Fellowships for Research in Japan (ID: S24075). T.E. was supported by the "Extreme Natural Phenomena" RIKEN Hakubi project and the JST Japan grant number JPMJFR202O (Sohatsu). N.O. was supported by the RIKEN Junior Research Associate Program. A.A. and S.I. were supported by the RIKEN Student Researcher Program.

Facilities: Swift, MAXI.

Software: HEASOFT.

ORCID iDs

Chin-Ping Hu https://orcid.org/0000-0001-8551-2002
Tomoshi Takeda https://orcid.org/0009-0008-5133-9131
Teruaki Enoto https://orcid.org/0000-0003-1244-3100
Toru Tamagawa https://orcid.org/0000-0002-8801-6263
Biswajit Paul https://orcid.org/0000-0002-8775-5945
Wataru Iwakiri https://orcid.org/0000-0002-0207-9010
Tatehiro Mihara https://orcid.org/0000-0002-6337-7943
Amira Aoyama https://orcid.org/0009-0008-3926-363X

References

Aoyama, A., Enoto, T., Takahashi, T., et al. 2025, ApJL, 986, L29
Barthelmy, S. D., Barbier, L. M., Cummings, J. R., et al. 2005, SSRv, 120, 143
Bildsten, L., Chakrabarty, D., Chiu, J., et al. 1997, ApJS, 113, 367
Brightman, M., Harrison, F. A., Bachetti, M., et al. 2019, ApJ, 873, 115
Brumback, M. C., Hickox, R. C., Fürst, F. S., et al. 2020, ApJ, 888, 125
Brumback, M. C., Vasilopoulos, G., Coley, J. B., Dage, K., & Miller, J. M. 2023, ApJ, 953, 89
Buccheri, R., Bennett, K., Bignami, G. F., et al. 1983, A&A, 128, 245
Cash, W. 1979, ApJ, 228, 939
Charles, P., Clarkson, W., Cornelisse, R., & Shih, C. 2008, NewAR, 51, 768
Clarkson, W. I., Charles, P. A., Coe, M. J., & Laycock, S. 2003a, MNRAS, 343, 1213
Clarkson, W. I., Charles, P. A., Coe, M. J., et al. 2003b, MNRAS, 339, 447
Dage, K. C., Brumback, M., Neilsen, J., et al. 2022, MNRAS, 514, 5457
Dage, K. C., Clarkson, W. I., Charles, P. A., Laycock, S. G. T., & Shih, I.-C. 2019, MNRAS, 482, 337
Doroshenko, V., Poutanen, J., Tsygankov, S. S., et al. 2022, NatAs, 6, 1433
Falanga, M., Bozzo, E., Lutovinov, A., et al. 2015, A&A, 577, A130
Forsblom, S. V., Tsygankov, S. S., Poutanen, J., et al. 2024, A&A, 691, A216
Fürst, F., Walton, D. J., Israel, G. L., et al. 2023, A&A, 672, A140
Gruber, D. E., & Rothschild, R. E. 1984, ApJ, 283, 546
Heyl, J., Doroshenko, V., González-Caniulef, D., et al. 2024, NatAs, 8, 1047
Hickox, R. C., & Vrtilek, S. D. 2005, ApJ, 633, 1064
Hu, C.-P., Chou, Y., Wu, M.-C., Yang, T.-C., & Su, Y.-H. 2011, ApJ, 740, 67
Hu, C.-P., Dage, K. C., Clarkson, W. I., et al. 2023, MNRAS, 520, 3436
Hu, C.-P., Mihara, T., Sugizaki, M., Ueda, Y., & Enoto, T. 2019, ApJ, 885, 123
Illarionov, A. F., & Sunyaev, R. A. 1975, A&A, 39, 185
Ínam, S., Baykal, A., & Beklen, E. 2010, MNRAS, 403, 378
Inoue, H. 2019, PASJ, 71, 36
Jahoda, K., Markwardt, C. B., Radeva, Y., et al. 2006, ApJS, 163, 401
Kaaret, P., Feng, H., & Roberts, T. P. 2017, ARA&A, 55, 303
Karam, R., Dage, K. C., Tetarenko, B. E., et al. 2025, MNRAS, 536, 509
King, A. R. 2008, MNRAS, 385, L113
Kong, A. K. H., Hu, C.-P., Lin, L. C.-C., et al. 2016, MNRAS, 461, 4395
Kosec, P., Pinto, C., Walton, D. J., et al. 2018, MNRAS, 479, 3978
Krimm, H. A., Holland, S. T., Corbet, R. H. D., et al. 2013, ApJS, 209, 14
Livingstone, M. A., Ransom, S. M., Camilo, F., et al. 2009, ApJ, 706, 1163
Lucke, R., Yentis, D., Friedman, H., Fritz, G., & Shulman, S. 1976, ApJL, 206, L25
Lyne, A. G., Jordan, C. A., Graham-Smith, F., et al. 2015, MNRAS, 446, 857
Matsuoka, M., Kawasaki, K., Ueno, S., et al. 2009, PASJ, 61, 999
Mihara, T., Nakajima, M., Sugizaki, M., et al. 2011, PASJ, 63, S623
Neilsen, J., Hickox, R. C., & Vrtilek, S. D. 2004, ApJL, 616, L135
Ogilvie, G. I., & Dubus, G. 2001, MNRAS, 320, 485
Ota, N., Takahashi, T., Tamagawa, T., et al. 2025, SPIE, 13625, 136250D
Paul, B., Nagase, F., Endo, T., et al. 2002, ApJ, 579, 411
Pradhan, P., Maitra, C., & Paul, B. 2020, ApJ, 895, 10
Pringle, J. E. 1996, MNRAS, 281, 357
Remillard, R. A., Loewenstein, M., Steiner, J. F., et al. 2022, AJ, 163, 130
Reynolds, A. P., Hilditch, R. W., Bell, S. A., & Hill, G. 1993, MNRAS, 261, 337
Scott, D. M., Leahy, D. A., & Wilson, R. B. 2000, ApJ, 539, 392
Staubert, R., Klochkov, D., Postnov, K., et al. 2009, A&A, 494, 1025
Staubert, R., Klochkov, D., Vasco, D., et al. 2013, A&A, 550, A110
Sugizaki, M., Mihara, T., Serino, M., et al. 2011, PASJ, 63, S635
Takeda, T., Tamagawa, T., Enoto, T., et al. 2025, PASJ, 77, L24
Tamagawa, T., Enoto, T., Kitaguchi, T., et al. 2025, PASJ, 77, 466
Trowbridge, S., Nowak, M. A., & Wilms, J. 2007, ApJ, 670, 624
van der Meer, A., Kaper, L., van Kerkwijk, M. H., Heemskerk, M. H. M., & van den Heuvel, E. P. J. 2007, A&A, 473, 523
Vasilopoulos, G., Lander, S. K., Koliopanos, F., & Bailyn, C. D. 2020, MNRAS, 491, 4949
Vasilopoulos, G., Petropoulou, M., Koliopanos, F., et al. 2019, MNRAS, 488, 5225
Verner, D. A., Yakovlev, D. G., Band, I. M., & Trzhaskovskaya, M. B. 1993, ADNDT, 55, 233
Walton, D. J., Fürst, F., Bachetti, M., et al. 2016, ApJL, 827, L13
Wilms, J., Allen, A., & McCray, R. 2000, ApJ, 542, 914
Wojdowski, P., Clark, G. W., Levine, A. M., Woo, J. W., & Zhang, S. N. 1998, ApJ, 502, 253